Self-Assembly of Isostatic Self-Dual Colloidal Crystals

Qun-Li Lei,[1,2,*] Wei Zheng,[1,2,*] Feng Tang,[1] Xiangang Wan,[1] Ran Ni,[2,†] and Yu-qiang Ma[1,‡]
[1]National Laboratory of Solid State Microstructures and School of Physics, Collaborative Innovation Center of Advanced Microstructures, Nanjing University, 210093 Nanjing, China
[2]School of Chemical and Biomedical Engineering, Nanyang Technological University, 62 Nanyang Drive, 637459 Singapore

(Received 8 March 2021; accepted 1 June 2021; published 29 June 2021)

Self-dual structures whose dual counterparts are themselves possess unique hidden symmetry, beyond the description of classical spatial symmetry groups. Here we propose a strategy based on a nematic monolayer of attractive half-cylindrical colloids to self-assemble these exotic structures. This system can be seen as a 2D system of semidisks. By using Monte Carlo simulations, we discover two isostatic self-dual crystals, i.e., an unreported crystal with *pmg* space-group symmetry and the twisted kagome crystal. For the *pmg* crystal approaching the critical point, we find the double degeneracy of the full phononic spectrum at the self-dual point and the merging of two tilted Weyl nodes into one *critically tilted* Dirac node. The latter is "accidentally" located on the high-symmetry line. The formation of this unconventional Dirac node is due to the emergence of the critical flatbands at the self-dual point, which are linear combinations of "finite-frequency" floppy modes. These modes can be understood as mechanically coupled self-dual rhombus chains vibrating in some unique uncoupled ways. Our work paves the way for designing and fabricating self-dual materials with exotic mechanical or phononic properties.

DOI: 10.1103/PhysRevLett.127.018001

Introduction.—Duality describes the hidden relationship between two seemingly different structures or descriptions [1,2], e.g., the graph duality in geometry [3], Kramers-Wannier duality [4], the electromagnetic duality [5], etc. Duality can generate a self-dual point, at which the dual counterpart of the structure is itself, and unique hidden symmetry emerges giving rise to some unusual degeneracy beyond the description of standard space-group theories [6–8]. Recently, a self-dual point was discovered in an isostatic mechanical network whose average coordination number is twice the system dimension, which can be used to realize the "mechanical spintronics" [9]. According to the Maxwell rule [10], this kind of structure is at the edge of mechanical stability (isostatic point) [11–14]. This property has been utilized to design flexible metamaterials [15–19] and topological mechanical insulators [20–25]. Nevertheless, so far, only twisted kagome lattice was found to be self-dual [9] and the origin of this duality remains unknown. Searching for new self-dual isostatic structures of different symmetries not only helps uncover the principle of duality in related classical systems, but also paves the way to fabricate exotic mechanical and/or phononic materials, for which one needs to find new strategies to construct microscopic structures with discrete dual transformations [9,26].

In this Letter, we show that a nematic monolayer of attractive half-cylindrical colloidal rods can self-assemble into two isostatic self-dual crystals with discrete freedom degrees, i.e., the twisted kagome crystal and an unreported crystal with *pmg* space-group symmetry. The hidden duality in the new isostatic structure induces the double degeneracy of the full phononic spectrum at the self-dual point and generates unconventional critically tilted Dirac cones, which are accidentally located on the high-symmetry lines in the Brillouin zone (BZ). As the system departs from the self-dual point, each Dirac node divides into two Weyl nodes. We find that the emergence of the critical flatbands at the self-dual point is the key to the formation of the critically tilted Dirac cones. These flatbands are linear combinations of the finite-frequency floppy modes, which can be understood as mechanically coupled self-dual rhombus chains vibrating in some unique uncoupled ways. Our finding can not only help build new self-dual materials with exotic mechanical or phononic properties, but also provide opportunities to observe intriguing phenomena in extreme conditions with simple classical systems.

Model and simulation.—We consider a monolayer of N hard half-cylindrical colloidal rods with diameter σ [Fig. 1(a)] and assume the rods are perfectly aligned under external fields or nematic interactions [27,28]. Except for the hard core interaction, there is also a short-range attraction between the curved lateral surfaces of two parallel rods, which we model as a square-well potential, with $w = 0.1\sigma$ the square-well width and ε the well depth. This attraction can be realized by depletion force [29] and capillary bridging force [30] with surface modifications or effective interaction arising from nematic liquid crystal elasticity [31,32]. We define a reduced temperature $T^* = k_B T/\varepsilon$, where k_B and T are the Boltzmann constant

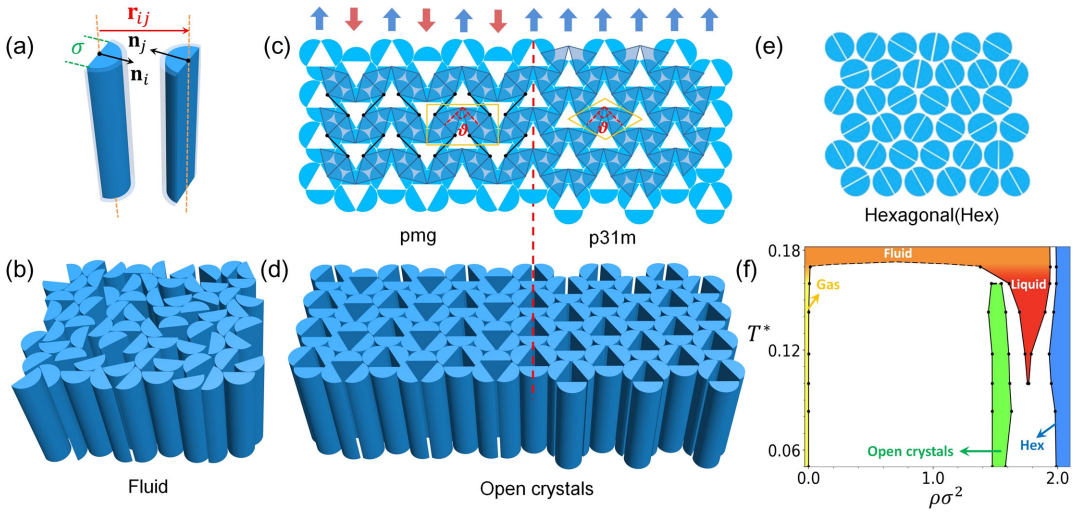

FIG. 1. (a) Schematic of two parallel half-cylindrical rods. (b) Fluid phase. (c),(d) Top and side views of open crystals in contact. Left: pmg crystal. Right: $p31m$ (twisted kagome) crystal, where ϑ is the open angle. The blue and red arrows indicate the orientation of the stripes. The orange lines enclose the unit cells of two crystals. (e) Hexagonal (Hex) crystal phase. (f) Phase diagram of the system in dimensions of density ρ and reduced temperature T^*.

and the temperature of system, respectively. Since the rods are perfectly aligned, the system can be effectively modeled as a 2D semidisk system. $\rho = N/A$ is the 2D density, with A the 2D area. We perform Monte Carlo simulations of the system with full periodic boundary conditions [28,33,34]. The details of the simulation can be found in the Supplemental Material [35].

Entropy-stabilized isostatic open crystals.—In Fig. 1(f), we show the obtained phase diagram of the system. At high T^*, the fluid phase [Fig. 1(b)] is a thermodynamically stable phase up to $\rho\sigma^2 \simeq 1.8$, while the hexagonal crystal phase [Fig. 1(e)] can only be stable when $\rho\sigma^2 \gtrsim 2.0$. The hexagonal crystal is a hierarchical structure consisting of dimers of two close-packed half-cylinders. With decreasing T^*, the fluid phase is divided into a dilute gas phase and a dense liquid phase. The critical regime of the gas-liquid phase separation is indicated by the dashed line in the phase diagram. With further decreasing T^*, the open crystal phase [Fig. 1(d)] appears between the gas and liquid phases. The latter finally disappears when $T^* \lesssim 0.1$. The phase diagram remains qualitatively the same when decreasing the attraction range (see Fig. S1 in the Supplemental Material [35]). As shown in Figs. 1(c) and 1(d), the open crystals are also hierarchical structures, which are composed of the half-cylindrical trimers with the triangle empty void. These trimers align in stripes whose direction can be up (A) and down (B) as indicated by the blue and red arrows in Fig. 1(c). We find the $AAAA$ sequence leads to the twisted kagome crystal with $p31m$ symmetry, while the $ABAB$ sequence produces an unreported crystal with pmg symmetry. The unit cells for the two open crystals are drawn in Fig. 1(c) using orange lines. Similar to the twisted kagome lattice, which can be obtained from the standard kagome lattice through twisting the unit cell (Guest-Hutchinson mode [41]), the pmg lattice can be formed from a rectangular lattice by doing a similar deformation (see Fig. S2 for the deformable pmg lattice assembled from Lego units in [35]). More importantly, the densities of both two crystals are controlled by the same open angle ϑ as shown in Fig. 1(c). Therefore, two crystals are compatible with each other on the phase boundary [see the dashed line in Fig. 1(c) and Fig. S3 in [35]]. The free energy of pmg crystals is only slightly lower than the $p31m$ crystal (about 0.03 k_BT per particle) due to the different vibrational entropy, according to free-energy calculations based on Einstein integration and dynamic matrix theory (see text and Table S1 in [35]). This explains why, in our direct Monte Carlo simulation, only the nucleation of random stripe sequences instead of perfect $p31m$ or pmg crystals is observed, similar to the nucleation of fcc-hcp crystals from hard-sphere fluids [42]. In experiments, one can use a prefabricated template to induce the growth of the preferred crystal [43,44].

For open crystals, each particle forms four attractive bonds with its neighbors, making them isostatic crystal according to the Maxwell rule. Therefore, both open crystals can be stretched to about 150% without energy cost or symmetry breaking when $T^* \to 0$ (see Fig. S4 in [35]). Nevertheless, our simulation shows that the equilibrium open angle is $\vartheta_{\mathrm{eq}} = 95.7°$ at zero pressure ($T^* = 10^{-5}$, $w = 10^{-2}\sigma$). In the Supplemental Material [35], we construct a mean-field theory to calculate the rotational entropy of rods as function of open angle ϑ. This mean-field theory predicts that the rotational entropy is maximized around $\vartheta_{\mathrm{eq}} = 92.2°$ for both open crystals, close to the measured value. Therefore, these two isostatic crystals are

mechanically stabilized by entropy [45–47]. It should be mentioned that ϑ_{eq} can be effectively tuned in the range from 89.7° to 95.7° by changing the attractive area on the half-cylinders (see Fig. S5 in [35]). As shown later, this range covers the critical open angle $\vartheta_c = 90°$ at which the structure is self-dual.

Duality of pmg crystals.—At low temperature, when particles only vibrate around the lattice, the open crystal can be described by an effective Hamiltonian under the harmonic approximation (see [35] for the derivation),

$$H_{\mathrm{eff}} = \sum_i \frac{k}{2}\mathbf{u}_i^2 + \frac{\kappa}{2}\sum_h \Delta\alpha_h^2 \tag{1}$$

where $\mathbf{u}_i$ ($\Delta\alpha_h$) is the translational (rotational) displacement of particle i (bond angle h) from its equilibrium value. Here the first term accounts for central-force attractive bonds and the second term describes the effective bond-bending rigidity arising from particle rotational entropy, with k and κ the corresponding effective spring constants. When $T^* \to 0$ and $w \to 0$, which corresponds to the low-temperature limit for system with general interaction, the bond-bending rigidity can be neglected compared with the central-force bond stiffness. We calculate the phononic spectrum $\omega(\mathbf{q})$ for the *pmg* crystal under this condition by solving the eigenvalue of the dynamic matrix (see the Supplemental Material [35] for details). In Figs. 2(a)–2(c), we show $\omega(\mathbf{q})$ under three different open angles, i.e., $\vartheta_c = 90°$ and $\vartheta_c \pm \Delta\vartheta$ with $\Delta\vartheta = 15°$. We observe the identical phononic spectrum for $\vartheta_c \pm \Delta\vartheta$ and the twofold degeneracy of the spectrum at the critical angle ϑ_c, similar to what was found in twisted kagome lattice [9]. This indicates that this critical angle is associated with a hidden symmetry that produces the same effect in spin 1/2 electronic systems according to Kramers theorem [9,48]. We further prove that there exists a dual transformation represented by the unitary matrix $\mathcal{U}$ between *pmg* lattices at two different open angles ϑ and ϑ^* [Fig. 2(d)], which satisfies

$$\mathcal{U}(\mathbf{q})D(\vartheta^*, -\mathbf{q})\mathcal{U}^{-1}(\mathbf{q}) = D(\vartheta, \mathbf{q}), \tag{2}$$

with $\vartheta^* = 2\vartheta_c - \vartheta$. Therefore, $\vartheta = \vartheta^* = \vartheta_c$ is the self-dual point. Here $D(\vartheta, \mathbf{q})$ is the dynamic matrix of the system at open angle ϑ. In $\mathcal{U}$, different rows with different colors correspond to different sites in the unit cell. One can see that $\mathcal{U}$ contains site exchange operation ($2 \to 6$, $3 \to 5$). It also contains the translation operator $\hat{T}_x = e^{-i\mathbf{q}\cdot\mathbf{a}_1}$ that shifts site 1 by one period in the x direction. Lastly, $\mathcal{U}$ contains fourfold rotation operators $r_{\blacksquare} = \left(\begin{smallmatrix} 0 & 1 \\ -1 & 0 \end{smallmatrix}\right)$ acting on the vibrational freedom degrees.

Critically tilted Dirac cone.—In Figs. 2(a)–2(c), the eigenmodes are double degenerated along the MX line in the BZ [Fig. 2(e)] at arbitrary ϑ. This degeneracy is due to the nonsymmorphic glide reflection symmetry in the x direction. With $\vartheta \to \vartheta_c$, the double-degenerated bands (1, 2) and bands (3, 4) along the MX line begin to contact at a point (the magenta circle) and form a completely flat band (orange line). The linear behavior around this point suggests that it is a Dirac node composed of two coincident Weyl nodes. To confirm this, we calculate the Berry phase

$$\gamma_j = i\oint_{\mathcal{C}} d\mathbf{q}\cdot\vec{\mathbf{u}}_j(\mathbf{q})\nabla_{\mathbf{q}}\vec{\mathbf{u}}_j^{\dagger}(\mathbf{q}) \tag{3}$$

along an enclosed trajectory $\mathcal{C}$ round the Dirac node in the BZ for band j, where $\vec{\mathbf{u}}_j(\mathbf{q})$ is the eigenstate at $\mathbf{q}$. For 2D Dirac (Weyl) systems, the Berry phase divided by π is a

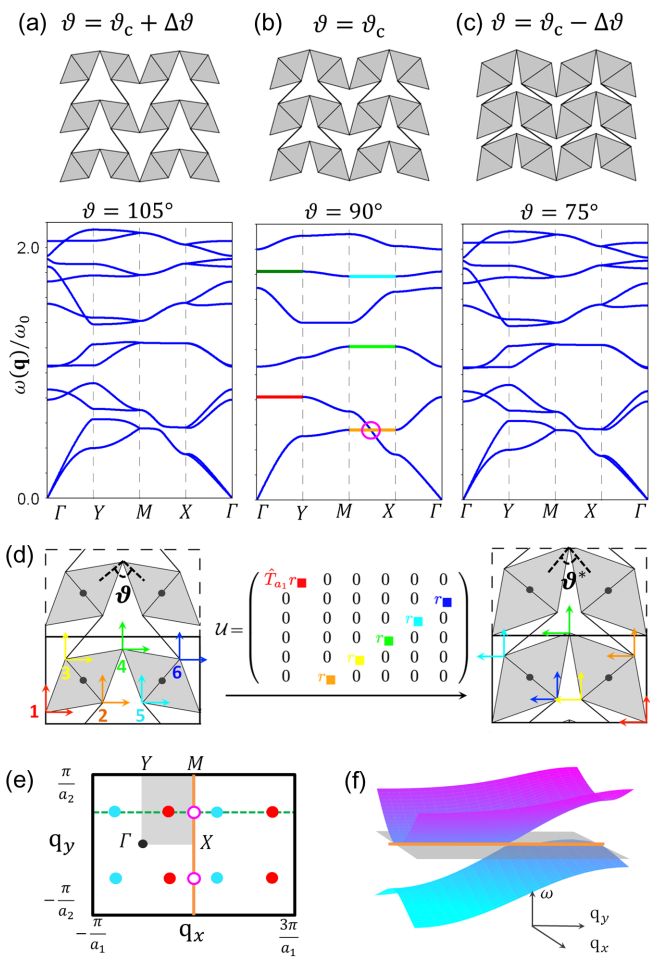

FIG. 2. (a)–(c) Phononic spectrum of *pmg* harmonic crystals at different open angles. The flatbands are indicated by different colors except blue. The Dirac node is marked by the magenta circle. (d) Duality transformation that maps the vibrational freedom degrees between two *pmg* lattices. Black dots are the centers of space inversion. (e) Two adjacent Brillouin zones separated by the orange line at $q_x = \pi/a_1$. The red (blue) sold points represent the tilted Weyl nodes with Berry phase $\pm\pi$, which merge into a critically tilted Dirac node (magenta circle) as $\vartheta \to \vartheta_c$. (f) 3D band surfaces of bands (1, 2) and bands (3, 4) near the critically tilted Dirac node.

quantized topological number (winding number) [49,50]. The Weyl nodes with Berry phase $\pm\pi$ can be viewed as topological charges or vortices with sign $\pm$ in the vector field of 2D momentum space [49]. We find that the Berry phase is $\pm\pi$ for either bands (1, 2) or bands (3, 4) when the trajectory encloses the node, while the summation of the two phases remains zero, indicating that topological charges neutralize at the Dirac node. On the contrary, the Berry phase remains zero when the trajectory does not enclose the nodes for all four bands. In Fig. 2(f), we also plot the 3D band surfaces of bands (1, 2) and bands (3, 4). We find that the contact point essentially connects two double-degenerated, critically tilted Dirac cones. The flatband along the MX line turns out to be the tangent line (orange line) of two bands with a horizontal surface (shadow plane). We notice that similar critically tilted Dirac (Weyl) cones, which are also called type III or zero-index Dirac (Weyl) cones, were recently discovered in electronic and phononic systems [51–56]. At this cone, the quasiparticles have highly isotropic mass, which can induce many interesting phenomena, like zero flection index [56], black hole horizon [54,57], and enhanced superconducting gap [58], etc. In our system, the Dirac node is protected by glide reflection and the hidden self-dual symmetry. Thus, changing the mass of particle pair (1, 4), (2, 6), or (3, 5) does not lift the Dirac nodes. Moreover, the Dirac nodes are located accidentally on a high-symmetry line. References [7,8] showed that the accidental degeneracy can result from the hidden antiunitary symmetry, which is consistent with the antiunitary nature of dual transformation [9].

As the system departing from the critical point, each Dirac node is separated into two noncritically tilted Weyl nodes with opposite Berry phases $\pm\pi$, which we represent as red (+) and blue (−) solid points in Fig. 2(e). These nodes are the contact points between bands (2, 3), which are hidden in Figs. 2(a) and 2(c). The dividing of one Dirac node into two Weyl points in our system is similar to the transition from Dirac semimetals to Weyl semimetals in electronic systems [59]. In 3D, the Weyl nodes can be accidentally generated at low-symmetry points in the BZ [59], while in 2D it would be impossible without additional symmetry constraints. In our system, we find that the Weyl nodes can be lifted by changing the mass of the particle pair (2, 6), (3, 5), (2, 5), or arbitrary single particle, but not for the particle pair (1, 4), (2, 3), or (5, 6). This suggests these nodes are protected by the space inversion symmetry with the center points marked as black dots in Fig. 2(d).

Critical flatbands and finite-frequency floppy modes.—When ϑ approaches ϑ_c, another interesting phenomenon is the emergence of double-degenerated flatbands, which are indicated by five different colors except blue in Fig. 2(b). As shown previously, the orange flatband is the key to the formation of the critically tilted Dirac cone. In Figs. 3(a) and 3(b), we show one of two eigenmodes for the M point and X point on this flatband, respectively. Their degenerated counterparts are shown in Fig. S6 in [35]. In the Supplemental Material [35], we prove that these flatbands are linear combinations of finite-frequency floppy modes in which vibration freedom degrees of linking bonds [thick lines in Fig. 3(a) and 3(b)] are frozen. Since these linking bonds contribute zero energy, these floppy modes are also the eigenmodes of the chain of rhombic units [see Fig. 3(c)]. In Figs. 3(d)–3(f), we plot the phononic spectrum of this chain system at three different open angles ϑ, as the same as that in Figs. 2(a)–2(c). We find the duality of the 2D lattice is preserved in this quasi-1D system, which results in the same double degeneracy of band structure at ϑ_c. Exact mapping can be built between the flatbands in Fig. 2(b) and the degenerated points in Fig. 3(e), which are marked by circles of the same colors. These findings suggest the possibility of designing high-dimensional self-dual structures from the low-dimensional ones [60].

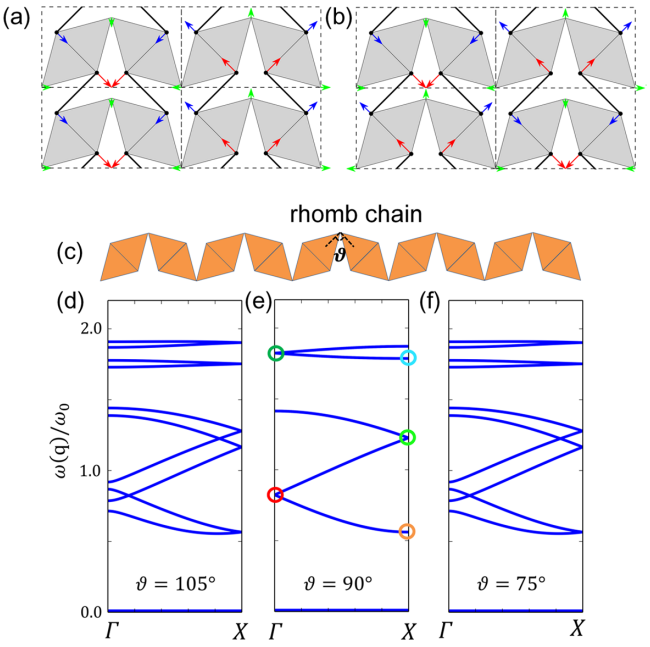

FIG. 3. (a),(b) Vibrational modes at X and M points in the BZ for the orange flatband. The vibration direction of linking points (red and blue arrows) are perpendicular to the linking bonds (thick black lines). (c) The structure of the chain of rhombic units. (d)–(f) Phononic spectrum of the chain at different open angles. The colored circles at Γ and X points correspond to the flatbands of the same colors in Fig. 2(b).

Conclusion and discussion.—By using Monte Carlo simulation, we demonstrate that half-cylindrical colloidal rods with short-range attraction can self-assemble into two isostatic self-dual crystals with $p31m$ (twisted kagome) and pmg symmetries. To the best of our knowledge, this special pmg isostatic structure has not been reported before, which exhibits unconventional critical-tilted Dirac cones and rare finite-frequency floppy modes. Since half-cylindrical geometry can be projected by a 2D semidisk pattern, one can

apply current mature techniques based on photolithography or mold to fabricate half-cylindrical rods [61–63]. This method can also be used to directly fabricate a 2D array of end-fixed half-cylindrical pillars, where the central-force bonds between pillars are realized by the screened electrostatic repulsion. Similar open crystals are also expected to be self-assembled from bowl- [64] or banana-shaped [65] colloidal particles with patchy modifications. Our finding opens up new possibilities in designing 2D metamaterials with exotic mechanical or phononic properties [17,18]. For example, the existence of the critically tilted Dirac cone in this self-assembled structure suggests that it is possible to fabricate zero-index phononic or mechanical materials in a cheaper and faster way [56,66]. It also provides opportunities in classical systems to observe some intriguing phenomena that commonly exist in extreme conditions, e.g., the black hole horizon [54,57,67].

This work is supported by the National Natural Science Foundation of China (Grants No. 11474155 and No. 11774147), by Singapore Ministry of Education through the Academic Research Fund MOE2019-T2-2-010 and RG104/17 (S), by Nanyang Technological University Start-Up Grant (No. NTU-SUG: M4081781.120), by the Advanced Manufacturing and Engineering Young Individual Research Grant (No. A1784C0018), and by the Science and Engineering Research Council of Agency for Science, Technology, and Research Singapore. We are grateful to the High Performance Computing Center (HPCC) of Nanjing University for supporting the numerical calculations.

*These authors contributed equally to this work.
†r.ni@ntu.edu.sg
‡myqiang@nju.edu.cn

[1] R. Savit, Duality in field theory and statistical systems, Rev. Mod. Phys. **52**, 453 (1980).
[2] F. Quevedo, Duality and global symmetries, Nucl. Phys. B, Proc. Suppl. **61**, 23 (1998).
[3] C. Berge, *The Theory of Graphs* (Dover Publications, Mineola, 2001).
[4] H. A. Kramers and G. H. Wannier, Statistics of the two-dimensional ferromagnet. Part I, Phys. Rev. **60**, 252 (1941).
[5] I. Fernandez-Corbaton, X. Zambrana-Puyalto, N. Tischler, X. Vidal, M. L. Juan, and G. Molina-Terriza, Electromagnetic Duality Symmetry and Helicity Conservation for the Macroscopic Maxwells Equations, Phys. Rev. Lett. **111**, 060401 (2013).
[6] T. Louvet, P. Delplace, A. A. Fedorenko, and D. Carpentier, On the origin of minimal conductivity at a band crossing, Phys. Rev. B **92**, 155116 (2015).
[7] J.-M. Hou and W. Chen, Hidden antiunitary symmetry behind accidental degeneracy and its protection of degeneracy, Front. Phys. **13**, 130301 (2018).
[8] J.-M. Hou, Hidden-Symmetry-Protected Topological Semimetals on a Square Lattice, Phys. Rev. Lett. **111**, 130403 (2013).
[9] M. Fruchart, Y. Zhou, and V. Vitelli, Dualities and non-Abelian mechanics, Nature (London) **577**, 636 (2020).
[10] J. Maxwell, On the calculation of the equilibrium and stiffness of frames, Philos. Mag. **27**, 294 (1864).
[11] A. Souslov, A. J. Liu, and T. C. Lubensky, Elasticity and Response in Nearly Isostatic Periodic Lattices, Phys. Rev. Lett. **103**, 205503 (2009).
[12] K. Sun, A. Souslov, X. Mao, and T. C. Lubensky, Surface phonons, elastic response, and conformal invariance in twisted kagome lattices, Proc. Natl. Acad. Sci. U.S.A. **109**, 12369 (2012).
[13] T. Lubensky, C. Kane, X. Mao, A. Souslov, and K. Sun, Phonons and elasticity in critically coordinated lattices, Rep. Prog. Phys. **78**, 073901 (2015).
[14] X. Mao and T. C. Lubensky, Maxwell lattices and topological mechanics, Annu. Rev. Condens. Matter Phys. **9**, 413 (2018).
[15] O. R. Bilal, R. Süsstrunk, C. Daraio, and S. D. Huber, Intrinsically polar elastic metamaterials, Adv. Mater. **29**, 1700540 (2017).
[16] J. Liu, Y. Nie, H. Tong, and N. Xu, Realizing negative Poisson's ratio in spring networks with close-packed lattice geometries, Phys. Rev. Mater. **3**, 055607 (2019).
[17] K. Bertoldi, V. Vitelli, J. Christensen, and M. Van Hecke, Flexible mechanical metamaterials, Nat. Rev. Mater. **2**, 17066 (2017).
[18] G. Ma, M. Xiao, and C. T. Chan, Topological phases in acoustic and mechanical systems, Nat. Rev. Phys. **1**, 281 (2019).
[19] J. McInerney, B. G. -g. Chen, L. Theran, C. D. Santangelo, and D. Z. Rocklin, Hidden symmetries generate rigid folding mechanisms in periodic origami, Proc. Natl. Acad. Sci. U.S.A. **117**, 30252 (2020).
[20] C. Kane and T. Lubensky, Topological boundary modes in isostatic lattices, Nat. Phys. **10**, 39 (2014).
[21] D. Z. Rocklin, B. G. -g. Chen, M. Falk, V. Vitelli, and T. Lubensky, Mechanical Weyl Modes in Topological Maxwell Lattices, Phys. Rev. Lett. **116**, 135503 (2016).
[22] H. C. Po, Y. Bahri, and A. Vishwanath, Phonon analog of topological nodal semimetals, Phys. Rev. B **93**, 205158 (2016).
[23] A. S. Meeussen, J. Paulose, and V. Vitelli, Geared Topological Metamaterials with Tunable Mechanical Stability, Phys. Rev. X **6**, 041029 (2016).
[24] N. P. Mitchell, L. M. Nash, and W. T. Irvine, Tunable band topology in gyroscopic lattices, Phys. Rev. B **98**, 174301 (2018).
[25] D. Zhou, L. Zhang, and X. Mao, Topological Boundary Floppy Modes in Quasicrystals, Phys. Rev. X **9**, 021054 (2019).
[26] S. Gonella, Symmetry of the phononic landscape of twisted kagome lattices across the duality boundary, Phys. Rev. B **102**, 140301(R) (2020).
[27] P. Sharma, A. Ward, T. Gibaud, M. F. Hagan, and Z. Dogic, Hierarchical organization of chiral rafts in colloidal membranes, Nature (London) **513**, 77 (2014).
[28] Q.-L. Lei, R. Ni, and Y.-Q. Ma, Self-assembled chiral photonic crystals from a colloidal helix racemate, ACS Nano **12**, 6860 (2018).
[29] D. J. Kraft, R. Ni, F. Smallenburg, M. Hermes, K. Yoon, D. A. Weitz, A. van Blaaderen, J. Groenewold, M. Dijkstra,

and W. K. Kegel, Surface roughness directed self-assembly of patchy particles into colloidal micelles, Proc. Natl. Acad. Sci. U.S.A. **109**, 10787 (2012).
[30] B. Bharti, D. Rutkowski, K. Han, A. Umesh Kumar, C. K. Hall, and O. D. Velev, Capillary bridging as a tool for assembling discrete clusters of patchy particles, J. Am. Chem. Soc. **138**, 14948 (2016).
[31] H. Mundoor, B. Senyuk, and I. I. Smalyukh, Triclinic nematic colloidal crystals from competing elastic and electrostatic interactions, Science **352**, 69 (2016).
[32] I. I. Smalyukh, Liquid crystal colloids, Annu. Rev. Condens. Matter Phys. **9**, 207 (2018).
[33] W. Zheng, Q.-l. Lei, Y.-q. Ma, and R. Ni, Hierarchical glass transition of hard hemidisks with local assemblies, Soft Matter **16**, 8108 (2020).
[34] Q. L. Lei, K. Hadinoto, and R. Ni, Role of local assembly in the hierarchical crystallization of associating colloidal hard hemispheres, Phys. Rev. Mater. **1**, 052601(R) (2017).
[35] See Supplemental Material at http://link.aps.org/supplemental/10.1103/PhysRevLett.127.018001 for details of Monte Carlo simulation, derivation of system's effective Hamiltonian and dynamic matrix, free-energy calculations, and mechanism of flatband, which includes Refs. [36–40].
[36] D. Frenkel and B. Smit, *Understanding Molecular Simulation: From Algorithms to Applications*, Vol. 1 (Elsevier, New York, 2001).
[37] D. Zwillinger, *CRC Standard Mathematical Tables and Formulae* (CRC Press, Boca Raton, 2002).
[38] W. K. Qi, J. de Graaf, F. Qiao, S. Marras, L. Manna, and M. Dijkstra, Phase diagram of octapod-shaped nanocrystals in a quasi-two-dimensional planar geometry, J. Chem. Phys. **138**, 154504 (2013).
[39] X. M. Mao, Entropic effects in the self-assembly of open lattices from patchy particles, Phys. Rev. E **87**, 062319 (2013).
[40] X. Mao and T. C. Lubensky, Coherent potential approximation of random nearly isostatic kagome lattice, Phys. Rev. E **83**, 011111 (2011).
[41] S. Guest and J. Hutchinson, On the determinacy of repetitive structures, J. Mech. Phys. Solids **51**, 383 (2003).
[42] D. Frenkel and A. J. Ladd, New Monte Carlo method to compute the free energy of arbitrary solids. Application to the fcc and hcp phases of hard spheres, J. Chem. Phys. **81**, 3188 (1984).
[43] A.-P. Hynninen, J. H. J. Thijssen, E. C. M. Vermolen, M. Dijkstra, and A. van Blaaderen, Self-assembly route for photonic crystals with a bandgap in the visible region, Nat. Mater. **6**, 202 (2007).
[44] A. van Blaaderen, R. Ruel, and P. Wiltzius, Template-directed colloidal crystallization, Nature (London) **385**, 321 (1997).
[45] X. Mao, A. Souslov, C. I. Mendoza, and T. C. Lubensky, Mechanical instability at finite temperature, Nat. Commun. **6**, 5968 (2015).
[46] H. Hu, P. S. Ruiz, and R. Ni, Entropy Stabilizes Floppy Crystals of Mobile DNA-Coated Colloids, Phys. Rev. Lett. **120**, 048003 (2018).
[47] X. M. Mao, Q. Chen, and S. Granick, Entropy favours open colloidal lattices, Nat. Mater. **12**, 217 (2013).
[48] M. J. Klein, On a degeneracy theorem of Kramers, Am. J. Phys. **20**, 65 (1952).
[49] R. De Gail, J.-N. Fuchs, M. Goerbig, F. Piéchon, and G. Montambaux, Manipulation of Dirac points in graphene-like crystals, Physica (Amstetrdam) **407B**, 1948 (2012).
[50] M. Goerbig and G. Montambaux, Dirac fermions in condensed matter and beyond, in *Dirac Matter* (Springer, New York, 2017), pp. 25–53.
[51] E. J. Bergholtz, Z. Liu, M. Trescher, R. Moessner, and M. Udagawa, Topology and Interactions in a Frustrated Slab: Tuning from Weyl Semimetals to $\mathcal{C} > 1$ Fractional Chern Insulators, Phys. Rev. Lett. **114**, 016806 (2015).
[52] M. Trescher, B. Sbierski, P. W. Brouwer, and E. J. Bergholtz, Quantum transport in Dirac materials: Signatures of tilted and anisotropic Dirac and Weyl cones, Phys. Rev. B **91**, 115135 (2015).
[53] H. Liu, J.-T. Sun, C. Cheng, F. Liu, and S. Meng, Photoinduced Nonequilibrium Topological States in Strained Black Phosphorus, Phys. Rev. Lett. **120**, 237403 (2018).
[54] H. Huang, K.-H. Jin, and F. Liu, Black-hole horizon in the Dirac semimetal $Zn_2In_2S_5$, Phys. Rev. B **98**, 121110(R) (2018).
[55] M. Milićević *et al.*, Type-III and Tilted Dirac Cones Emerging from Flat Bands in Photonic Orbital Graphene, Phys. Rev. X **9**, 031010 (2019).
[56] F. Zangeneh-Nejad and R. Fleury, Zero-Index Weyl Metamaterials, Phys. Rev. Lett. **125**, 054301 (2020).
[57] H. Liu, J.-T. Sun, C. Song, H. Huang, F. Liu, and S. Meng, Fermionic analogue of high temperature Hawking radiation in black phosphorus, Chin. Phys. Lett. **37**, 067101 (2020).
[58] D. Li, B. Rosenstein, B. Y. Shapiro, and I. Shapiro, Effect of the type-I to type-II Weyl semimetal topological transition on superconductivity, Phys. Rev. B **95**, 094513 (2017).
[59] X. Wan, A. M. Turner, A. Vishwanath, and S. Y. Savrasov, Topological semimetal and Fermi-arc surface states in the electronic structure of pyrochlore iridates, Phys. Rev. B **83**, 205101 (2011).
[60] B. G. -g. Chen, B. Liu, A. A. Evans, J. Paulose, I. Cohen, V. Vitelli, and C. D. Santangelo, Topological Mechanics of Origami and Kirigami, Phys. Rev. Lett. **116**, 135501 (2016).
[61] M. Khorasaninejad and F. Capasso, Metalenses: Versatile multifunctional photonic components, Science **358**, eaam8100 (2017).
[62] M. Khorasaninejad, W. T. Chen, R. C. Devlin, J. Oh, A. Y. Zhu, and F. Capasso, Metalenses at visible wavelengths: Diffraction-limited focusing and subwavelength resolution imaging, Science **352**, 1190 (2016).
[63] Z. Hao *et al.*, Vertically aligned and ordered arrays of 2D MCo2S4@ metal with ultrafast ion/electron transport for thickness-independent pseudocapacitive energy storage, ACS Nano **14**, 12719 (2020).
[64] M. Marechal, R. J. Kortschot, A. F. Demirörs, A. Imhof, and M. Dijkstra, Phase behavior and structure of a new colloidal model system of bowl-shaped particles, Nano Lett. **10**, 1907 (2010).

[65] C. Fernández-Rico, M. Chiappini, T. Yanagishima, H. de Sousa, D. G. A. L. Aarts, M. Dijkstra, and R. P. A. Dullens, Shaping colloidal bananas to reveal biaxial, splay-bend nematic, and smectic phases, Science **369**, 950 (2020).

[66] I. Liberal and N. Engheta, Near-zero refractive index photonics, Nat. Photonics **11**, 149 (2017).

[67] G. E. Volovik, Black hole and Hawking radiation by type-II Weyl fermions, JETP Lett. **104**, 645 (2016).